symmetry

MDPI

Review

Review on the Reconstruction of Transition Dipole Moments by Solid Harmonic Spectrum

Yue Qiao [1,2,3], Jiaqi Chen [4] and Jigen Chen [1,*]

[1] Zhejiang Provincial Key Laboratory for Cutting Tools, Taizhou University, Jiaojiang District, Taizhou 318000, China
[2] Institute of Atomic and Molecular Physics, Jilin University, Changchun 130012, China
[3] Jilin Provincial Key Laboratory of Applied Atomic and Molecular Spectroscopy, Jilin University, Changchun 130012, China
[4] School of Materials Science and Engineering, Taizhou University, Jiaojiang District, Taizhou 318000, China
* Correspondence: kiddchen@126.com

Abstract: In the process of intense laser–matter interactions, the transition dipole moment is a basic physical quantity at the core, which is directly related to the internal structure of the solid and dominates the optical properties of the solid in the intense laser field. Therefore, the reconstruction of the transition dipole moment between solid energy bands is extremely important for clarifying the ultrafast dynamics of carriers in the strong and ultrashort laser pulse. In this review, we introduce recent works of reconstructing transition dipole moment in a solid, and the advantages and drawbacks of different works are discussed.

Keywords: solid high-order harmonic; transition dipole moments; reconstruction

Citation: Qiao, Y.; Chen, J.; Chen, J. Review on the Reconstruction of Transition Dipole Moments by Solid Harmonic Spectrum. *Symmetry* **2022**, *14*, 2646. https://doi.org/10.3390/sym14122646

Academic Editor: Tomohiro Inagaki

Received: 14 November 2022
Accepted: 12 December 2022
Published: 14 December 2022

1. Introduction

With the rapid development of laser technology, the laser amplitude has reached the Coulomb field strength that can be felt by the electrons in atoms. When such an intense laser field interacts with the matter, a series of nonlinear optical processes are generated [1–5], involving high-order harmonic generation (HHG) [6,7]. The coherent radiation frequency emitted by this process is tens or even hundreds of times that of the driving laser field, which can be used to produce coherent light sources in the bands of extreme ultraviolet (XUV) and soft x-ray. Moreover, due to the large bandwidth of its emission spectrum, high-order harmonic emission is also one of the main means to obtain optical pulses with attosecond (10^{-18}s) duration [8,9]. The ultrashort attosecond pulse can obtained by superimposing harmonic within a certain energy range. The intensity of the attosecond pulse in the time domain can be expressed as $I(t)=\left|\int_q a_q e^{iq\omega_0 t}\right|^2$, where $a_q=\int a(t)e^{-iq\omega_0 t}dt$, q is the order of harmonics, and $a(t)$ represents the time-dependent dipole acceleration of the system [10]. In 1993, Corkum et al. proposed a semi-classical "three-step model" to explain the HHG phenomenon of atoms and molecules [11]. According to the generation mechanism of HHG, it is known that the harmonic spectrum carries the structural properties and ultrafast dynamics information of the material during the emission process, so it can be used to detect the structural information on the sub-atomic space scale and the ultrafast dynamic process on the sub-femtosecond and even attosecond time scales [12].

Before the first observation of the non-perturbative HHG of ZnO crystal in 2011 [13], the research on HHG mainly focused on gas media [14–17]. However, the gaseous HHG has some limitations. The low conversion efficiency makes it difficult to directly apply the generated harmonic spectrum to observe and manipulate electronic processes. Compared with gas media, solids have the characteristics of high electron density, multi-center periodic potential, and delocalized Bloch wave packets, where electrons ionized from one atomic position in the periodic potential may recombine at any other position, resulting

in HHG with much higher efficiency. Therefore, the solid HHG has boomed over the past decade [18,19]. HHG has been observed in many solid materials, including MgO [20], ZnO [21,22], GaAs [23,24], GaN [25], GaSe [26,27], SiO_2 [28,29], ZnSe [30], MoS_2 [31,32], h-BN [33], graphene [34,35], and rare-gas solids of Ar and Kr [36]. Recently, HHG of solid-state systems containing impurities has been studied both experimentally [37] and theoretically [38,39]. Solid HHG has novel characteristics different from gaseous HHG. For example, the harmonic spectrum has a multi-platform structure, the cutoff energy is linearly related to the peak amplitude of the incident laser field, and there is a special correspondence between the generated harmonic ellipticity and the incident laser pulse [13,40–42]. Solid HHG can also detect Berry curvature [43,44], band structure [45–47], and topological effects [48,49].

Similar to the generation mechanism of gaseous HHG, Vamp et al. proposed a "three-step model" of solid-HHG on the basis of the framework of energy band theory [50]: (1) When irradiated by a laser pulse, electrons have the opportunity to transit from the valence band to the conduction one and then generate electron–hole pairs; (2) electrons and holes are driven by the laser electric field to do intraband Bloch oscillations in conduction and valence bands, respectively, and generate intraband currents; (3) when the phase accumulated during the propagation in bands satisfies the stationary phase condition, electrons and holes will recombine and release high-energy photons with energy corresponding to the instantaneous band gap, where the efficiency of the photons depends largely on the transition dipole moment (TDM) between the different energy bands. From the above generation mechanism of the solid HHG, it can be seen that the spectrum implies the spatial configuration and electronic structure information of the target itself.

Yu et al. investigated the dependence of the harmonic emission of SiO_2 crystals on the TDM [29]. By comparing the shape of the TDM and the corresponding harmonic spectrum obtained from the first-principles and the first-order k · p theory, they found that the harmonic conversion efficiency and cut-off energy increase significantly when the TDMs change greatly along a valley in the k direction of the crystal. Zhao et al. found that there is a minimum structure in the harmonic spectrum of the MgO crystal [51], which is similar to that of atoms and molecules. Further studies showed that it comes from the minimum value of the TDM between the valence band and the conduction one. This HHG minimum is also found in the works of Jiang et al. [52] and Tancogne-Dejean et al. [53]. The above research further proves that the k-dependent TDM plays an important role in solid HHG. Therefore, it is possible to reconstruct the solid TDM by the solid HHG.

According to the strong field approximation model [50,54], the solid interband harmonics in the low ionization approximation can be described as $D_{er}(\omega)=\omega \int_{BZ} d^3k\mathrm{d}(k) \int_{-\infty}^{\infty} dte^{-i\omega t} \int_{-\infty}^{t} dt^{'} F(t^{'})d^*(\kappa_{t^{'}}) \times e^{-iS(k,t^{'},t)-(t-t^{'})/T_2} + c.c.$, where the action $S(k,t^{'},t)= \int_{t^{'}}^{t} \varepsilon_{cv}(\kappa_\tau)d\tau$, and $\kappa_{t^{'}} = k - \mathrm{A}(t) + \mathrm{A}(t^{'})$. $\varepsilon_{cv}(\kappa_\tau)$ represents the band gap, $F(t^{'})$ is the laser pulse. $d(k)$ is TDM, and $d^*(k)$ represents conjugate of TDM. It can be noticed that the interband current is related to the laser field, the band gap, and TDM. In addition, Ref. [55] gives the formulas for the HHG yield including TDM. They showed that the interband HHG yield is inversely proportional to the band gap and proportional to the TDM. This indicates that a solid harmonic spectrum is a potential tool for retrieving k-dependent or energy-dependent TDM.

In addition, due to the important role of TDM in light–matter interaction, many methods for measuring TDM modulus and direction have been developed experimentally. In experiments, the TDM modulus of Eu^{3+}: Y_2SiO_5 was measured by the single-frequency hole-burning spectrum [56]. Through the transient absorption spectroscopy with polarization detection, combined with different techniques, for example, fluorescence spectroscopy and Fourier transforms infrared spectroscopy, the direction of TDM in isotropic samples can be obtained [57,58]. However, these methods cannot retrieve k-dependent or energy-dependent TDM. In addition, relatively speaking, HHG is a powerful tool for retrieving k-dependent or energy-dependent TDM.

In the following, we will introduce some recent works on k-dependent TDM reconstruction using the crystal harmonic spectrum from four aspects. These studies have guiding significance for the experimental measurement of the k-dependent TDM.

2. Reconstruction of TDM by Using Continuous Harmonic Spectrum

In 2019, Zhao et al. first proposed a method for the all-optical reconstruction of TDM, that is, using crystal harmonics under ultrashort laser pulses to reconstruct k-dependent TDM [59]. On the basis of the energy band structure and the TDM from the valence band and the conduction band, which was obtained by the first-principles calculation, they investigated the HHG of a MgO crystal driven by an ultrashort monochromatic laser field by solving the semiconductor Bloch equation (SBEs), and they demonstrated that the TDM between the conduction band and the valence one of the MgO crystal can be reconstructed by the supercontinuum harmonic generated by a single quantum trajectory. Based on Keldysh 's method, they gave a proportional relationship between the TDM and the interband HHG yield produced by a single quantum trajectory:

$$D_{er}(k_r) \propto \left| d_{cv}(k_r) e^{-(t_r - t_i')/T_2} \right|^2 \quad (1)$$

Here, t_r and t_i' represent recombination and ionization times, and k_r is the crystal momentum where recombination occurs. According to the emission mechanism of interband harmonics, the harmonic emission energy is equal to the band gap, which is determined by the crystal momentum when electrons recombine with holes. Therefore, the correspondence between the emitted energy and the momentum of crystal can be established, so that the harmonic energy can correspond to the TDM. Figure 1a shows the ultrashort pulse electric field that they adopted, and the corresponding laser parameters are depicted in the caption. The harmonic spectrum generated by the laser field of Figure 1a is given in Figure 1c. It can be seen that the harmonic spectrum of MgO is a continuous spectrum when driven by the ultrashort pulse, and the minimum structure caused by TDM can be observed around 16 eV in the harmonic spectrum. Figure 1b gives the corresponding time–frequency analysis and the classical trajectory from the photon energy and the emission instant. It can be observed that the quantum and classical trajectories are in good agreement, which proves that the harmonics are emitted by a single quantum trajectory. Therefore, the TDM can be reconstructed by Equation (1), and the reconstruction results are displayed in Figure 1d. The black dotted line represents the target TDM which is calculated by VASP, and the orange diamond is the TDM reconstructed by Equation (1). One can notice that the TDM reconstructed by this method is in good agreement with the target TDM at most k points.

In 2022, based on the work of Zhao et al., Qiao et al. extended the reconstruction of MgO crystal TDMs from two-band to three-band by using two-color laser pulses of 1700–5100 nm [60]. Figure 2a shows the total harmonic spectrum, interband, and intraband harmonic spectra of the three-band model driven by a two-color pulse. It can be found from the figure that the harmonics above the minimum band gap are mainly dominated by interband harmonics, and the harmonics of both platforms are supercontinuum. Figure 2b further exhibits the HHG spectra between different bands under the three-band model. The first platform of the harmonic spectrum is mainly induced by the harmonic between the valence and first conduction bands (VC_1), and the harmonic between the valence and the second conduction bands (VC_2) dominates the second plateau. The harmonic between the first conduction band and the second one (C_1C_2) has little effect on the two harmonic platforms above the minimum band gap. This indicates that the harmonic coupling between VC_1 and VC_2 is very small above the minimum band gap, and the interband current between other bands has little impact on them. Therefore, according to Equation (1), the harmonic spectra of the two platforms emitted from a single trajectory can be applied to image the TDMs of VC_1 and VC_2, respectively. The corresponding results are displayed in Figure 3. Through this scheme, the TDMs of VC_1 and VC_2 can be both well reconstructed by the continuum harmonic spectra.

Both of the above works use a few-cycle driving laser to generate the harmonic of a single quantum trajectory to retrieve the TDMs between different energy bands. This method has strict requirements for the laser pulse width, and it is less operable for experiments. However, the reconstructed TDM is consistent with the real TDM at most k points.

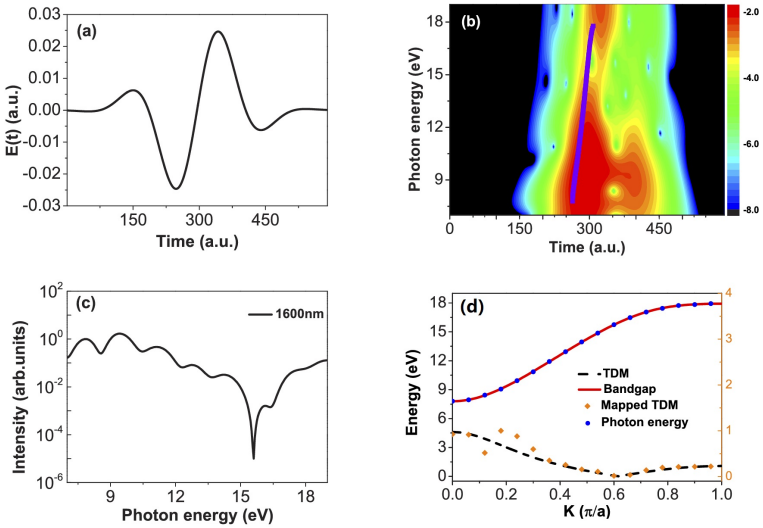

Figure 1. (**a**) The ultrashort laser field; (**b**) the time−frequency of the harmonic spectrum, the purple solid line represents the relationship between the emission energy and the emission time obtained by classical method; (**c**) the harmonic spectrum generated by the laser pulse in (**a**); (**d**) comparison of the TDM (black dotted line) obtained by first-principles with the TDM (orange diamond) reconstructed by the harmonic spectrum. The center wavelength of the laser is 1600 nm, the full width at half maximum is 5 fs, the carrier phase is 0, and the peak intensity is 3.0×10^{13} W/cm^2. They are reprinted with permission from Ref. [59] © The Optical Society.

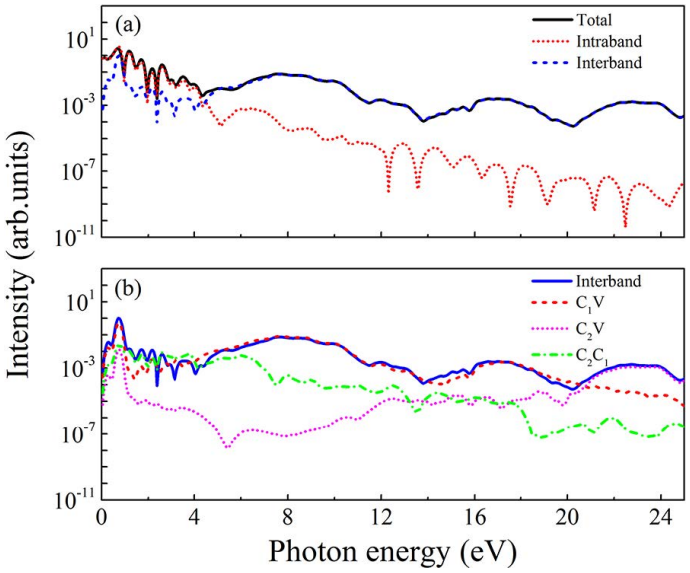

Figure 2. (**a**) The total harmonic spectrum of the three-band model (black solid line) and the HHG obtained by intraband current (red dotted line) and interband polarization (blue dashed line); (**b**) total interband HHG (blue solid line), harmonic spectrum between VC_1 (red dashed line), harmonic spectrum of VC_2 (pink dotted line), and harmonic spectrum from C_1C_2 (green dash-dotted line). Laser parameters: 1700–5100 nm, 2.1×10^{13} W/cm^2−0.525×10^{13} W/cm^2, the full width at half maximum is 11.34 fs. They are reprinted with permission from Ref. [60] © The Optical Society.

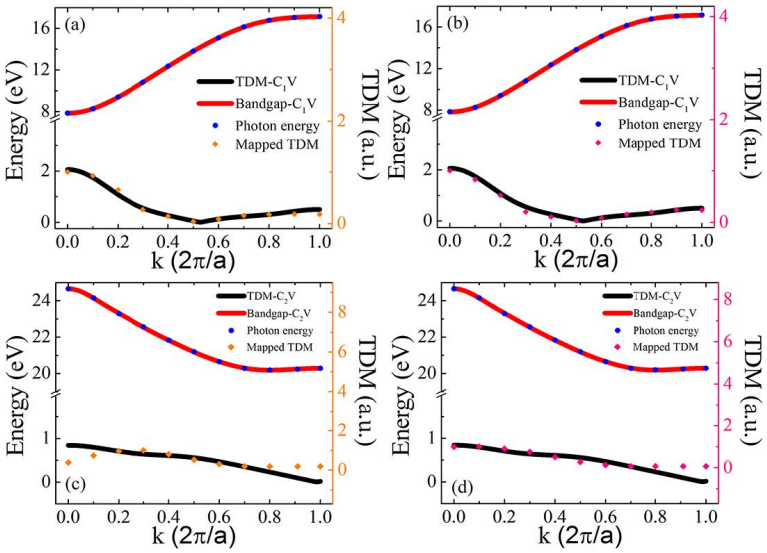

Figure 3. The reconstructed TDM (diamonds) of VC_1 by (**a**) directly or (**b**) indirectly adopting the harmonic spectra. The reconstructed TDM (diamonds) between VC_2 by (**c**) directly or (**d**) indirectly adopting the harmonic spectra. The blue circles are harmonic energy for mapping TDM. The black solid lines represent TDMs of VC_1 and VC_2 obtained by the first-principles, and the red solid lines are band gaps of VC_1 and VC_2 obtained by the first-principles. They are reprinted with permission from Ref. [60] © The Optical Society.

3. Reconstruction of TDM by Using the Harmonic Spectrum from a Multicycle Pulse

In 2022, Wu et al. proposed a scheme for reconstructing TDM through the harmonic spectra from multicycle pulses [61]. They studied the HHG of the crystals with symmetric and asymmetric under multicycle pulses by the SBEs. They found that the phase of the crystal TDM is relevant with the intensity ratio of the adjacent odd and even harmonics, and the crystal TDM modulus correlates with the adjacent odd harmonics. Through these relationships, they successfully imaged the TDMs of symmetric and asymmetric crystals. In an optical period of the multicycle laser pulse, there are two main emissions $[D_1(t), D_2(t + T_0/2)]$, which are generated by the ionized electrons near the instantaneous maximum of the incident electric field. Therefore, the intensity of N-order HHG can be expressed as:

$$\begin{aligned} I_N &= |D_1(\omega) + D_2(\omega)|^2 \\ &\propto \left| d^*(k_r) d(k_i') F(t_i') e^{(t_r - t_i')/T_2} (1 - e^{i(\Delta S - N\pi)}) \right|^2 \end{aligned} \tag{2}$$

When the electron excitation occurs near the Γ point and happens at the moment around the electric field peak, the TDM modulus of the symmetric crystal can be obtained by the intensity ratio of the adjacent odd harmonics:

$$\frac{I_{2n-1}}{I_{2n+1}} = \left| \frac{d\left(k_r{}^{2n-1}\right)}{d\left(k_r{}^{2n+1}\right)} \right|^2 \tag{3}$$

The results of the symmetric crystal obtained by Equation (3) are displayed in Figure 4b as the pink solid point. Compared with the TDM of target (blue dash-dotted line), the mapped TDM is consistent with the target TDM at most k points.

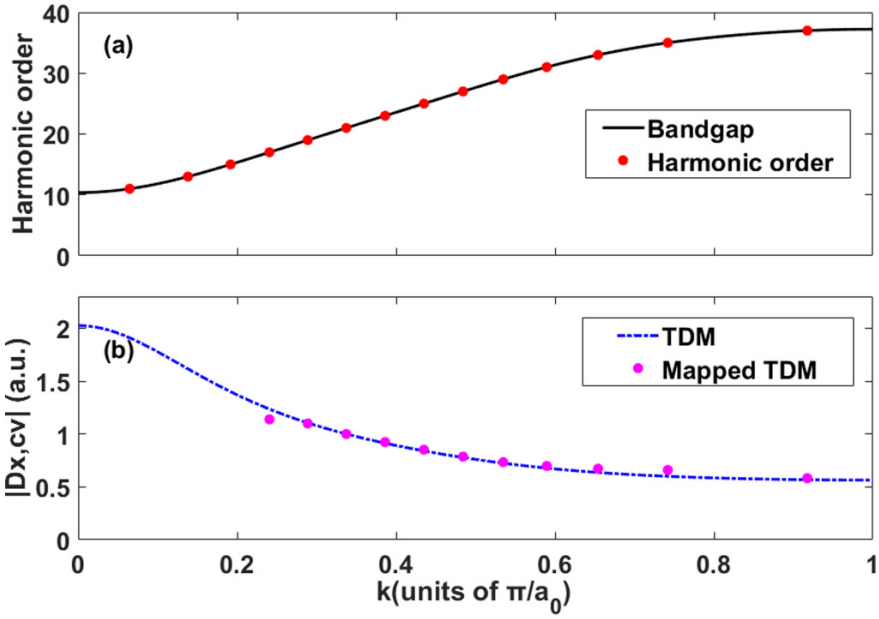

Figure 4. (**a**) The mapping relationship between harmonic order and lattice momentum. The red solid point represents the sampling point extracted from the harmonic spectrum, and the black solid line is the band gap of the symmetric crystal; (**b**) Target TDM (blue dash-dotted line) and reconstructed TDM (pink solid point). Reprinted figure with permission from [61] Copyright (2022) by the American Physical Society.

For asymmetric crystals, in addition to retrieving the TDM modulus, the phase of the TDM cannot be ignored too. Based on the intensity ratio of the adjacent odd-even harmonics, the phase of the TDM can be obtained by:

$$\frac{I_{2n}}{I_{2n+1}} = \tan^2\theta(k_r^{2n+1}) \tag{4}$$

Then, after inserting Equation (4) into Equation (3), the TDM modulus of asymmetric crystals can be obtained by:

$$\frac{I_{2n-1}}{I_{2n+1}} = \left| \frac{d\left(k_r{}^{2n-1}\right)\cos\left[\theta(k_r^{2n-1})\right]}{d\left(k_r{}^{2n+1}\right)\cos\left[\theta(k_r^{2n+1})\right]} \right|^2 \tag{5}$$

The results of the asymmetric crystals reconstructed by Equations (4) and (5) are exhibited in Figure 5a,b, respectively. In order to compare their results, they used three different transition dipole phases. It can be found that, compared with the target, the mapping result is consistent with the target at most k points.

Their work demonstrated that the reconstruction of TDM modulus and phase from symmetric and asymmetric crystals can be achieved by the harmonic spectra from the multicycle laser field. They solved the limitation of the laser pulse width and verified the universality of their scheme in a small range of the laser field strength. However, their result showed that the TDM corresponding to the position with a smaller k is difficult to reconstruct.

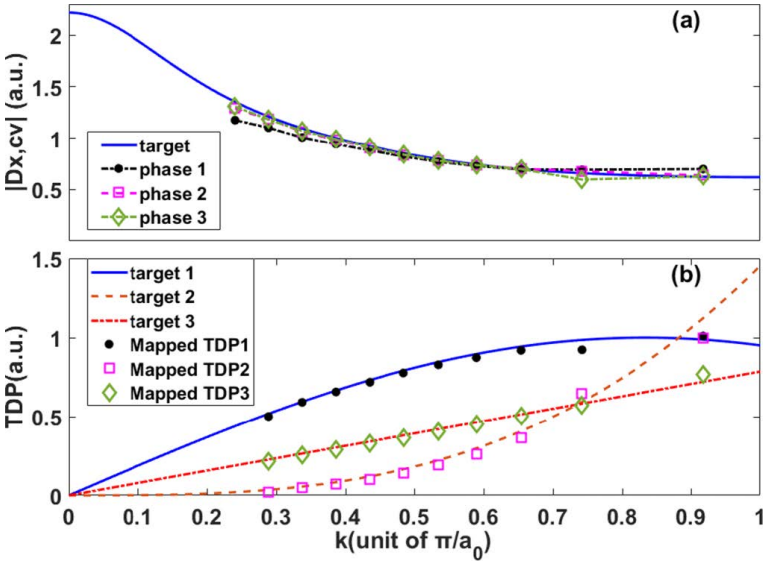

Figure 5. (**a**) The TDM modulus (blue solid line) of target and reconstructed TDM modulus (black circle, pink square, and green diamond) under different transition dipole phases; (**b**) target transition dipole phase (blue solid line, orange dotted line, and red dotted line) and mapped transition dipole phase (black circle, pink square, and green diamond). Reprinted figure with permission from [61] Copyright (2022) by the American Physical Society.

4. Reconstruction of TDM by Using the Polarization-Resolved HHG Excited by Band Gap Resonance

In 2021, Uchida et al. imaged the TDM texture of 2D thin-layer bulk black phosphorus based on polarization-resolved HHG excited by band gap resonance in the experiment [62]. In the range from mid-infrared to visible light, the absorption coefficient of the laser polarization along the armchair (AC) direction of the black phosphorus crystal is larger than that along the zigzag (ZZ) direction. Linear dichroism is the name for this absorption anisotropy, and it can be adopted as a probe for the orientation of the black phosphorus crystal. When the incident light resonates with the band gap, the band edge k_i can create electron–hole pairs selectively. The generated electron–hole pairs accelerate along the direction of the driving field and then recombine. When the contribution of intraband current in the HHG proceeding is much lower than that of the interband current, and when the recombination occurs, the TDM determines the HHG polarization and HHG amplitude. At this time, the interband current and the TDM satisfy the following approximate relationship:

$$d^*_{cv} \propto D_{er}(\omega)/\alpha(\theta, F_0, \omega, \Omega) d_{cv}(k_i) \cdot F_0 \quad (6)$$

Here, $\alpha(\theta, F_0, \omega, \Omega)$ depicts electron–hole recombination dynamics. The detailed description of $\alpha(\theta, F_0, \omega, \Omega)$ can be found in Ref. [62]. In a simple band structure, α can be supposed to be nearly invariant with respect to the direction of k_r where recombination occurs, i.e., driving laser polarization angle θ. Therefore, by measuring the crystal orientation dependence of the HHG yield and polarization, TDM between conduction and valence bands $d^*_{cv}(k)$ can be completely reconstructed on the isoenergetic line. Figure 6 shows the reconstructed TDM texture on the isoenergetic lines of the 3rd, 5th, 7th, and 9th harmonic emission energies.

Although the above method cannot give the absolute value of TDM, it can evaluate the relative amplitude and direction of the TDM on the isoenergetic line. In addition, their scheme can be verified by experiments, which is very valuable.

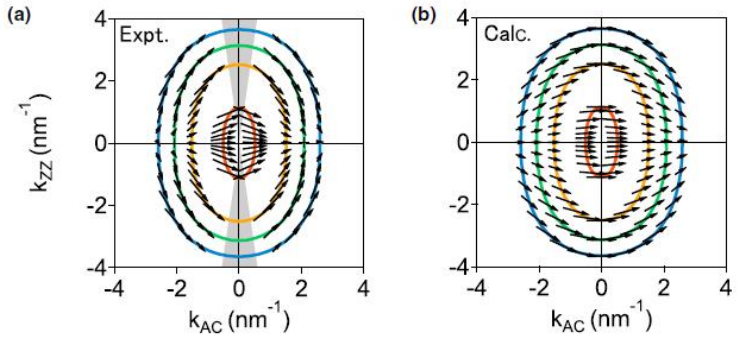

Figure 6. (**a**) The TDM texture obtained by the experiment. The Z point is set as the origin. The red, orange, green, and blue solid lines represent the isoenergetic lines corresponding to the 3rd (0.8 eV), 5th (1.3 eV), 7th (1.8 eV), and 9th (2.3 eV) harmonic emission energies, respectively. The gray shadow area represents the area where TDM cannot be obtained caused by the low signal-to-noise ratio; (**b**) the TDM texture obtained by calculation. Reprinted figure with permission from [62] Copyright (2022) by the American Physical Society.

5. Reconstruction by Using the Harmonic Spectrum and the TDM of a Reference Target

In 2020, Hoang et al. investigated the harmonic emission process of impurity-doped materials under intense laser fields using the time-dependent Schrödinger equation, and they found that there is a close relationship between harmonics and TDM [63]. Based on this connection, they retrieved the TDM of impurity-doped materials through the harmonic spectrum and the reference target TDM. When HHG from the impurity is dominant, the HHG yield of the impurity-doped material can be regarded as the product of a return electron "wave packet" and the TDM for electrons in the conduction bands returning to the ground state of the impurity:

$$D(\omega) \propto |W(\omega)d(\omega)|^2 \tag{7}$$

Moreover, under the same laser parameters, "wave packets" of different targets are almost identical as a function of the energy. The relation between the wave packet of the reference system and the wave packet of the impurity-doped system can be expressed as:

$$|W(\omega)|^2 = C\left|W_{ref}(\omega)\right|^2 \tag{8}$$

Here, C is an overall constant. When the HHG spectrum of the unknown impurity target and the reference system irradiated by the same laser is obtained, the TDM of the unknown impurity target can be extracted by the following formula:

$$|d(\omega)|^2 = C^{-1}\left|d_{ref}(\omega)\right|^2 \frac{D(\omega)}{D_{ref}(\omega)} \tag{9}$$

The corresponding results are given in Figure 7. It can be noticed that the TDMs retrieved by the HHG spectra under different laser parameters are in good agreement with the theoretical calculation of the TDM, and the position of the minimum value is also well reproduced.

Their work is an initial attempt to extend the quantitative rescattering theory from gas to solid. The advantage of their work is that they are not limited by laser parameters and can achieve single-shot measurement in principle. However, their scheme was obtained under ideal conditions for the impurity HHG dominant spectrum.

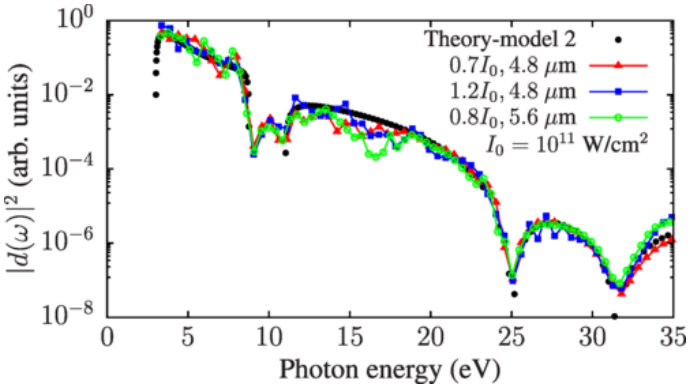

Figure 7. The retrieved energy-dependent TDMs between the impurity ground state and conduction band by using HHG with different laser parameters. The black solid point represents the target TDM. Reprinted figure with permission from [63] Copyright (2022) by the American Physical Society.

6. Conclusions

We review the recent works on the reconstruction of k-dependent TDM in crystals, all of which are achieved through the solid harmonic spectra. These works may have some limitations, but they are of great significance for the development of HHG detection technology. We expect more related research in the future. For example, expanding the TDM reconstruction to multiple dimensions, all-optical mapping scheme in a single shot measurement, and looking forward to the development of theoretical methods for the case of correlated electrons. Moreover, these schemes proposed at present need to take effect when interband harmonics play a major role. How to realize TDM reconstruction under any mechanism still needs to be further solved.

Author Contributions: Conceptualization, J.C. (Jigen Chen); writing—original draft preparation, Y.Q.; writing—review and editing, Y.Q. and J.C. (Jigen Chen); supervision, J.C. (Jiaqi Chen) and J.C. (Jigen Chen). All authors have read and agreed to the published version of the manuscript.

Funding: This work was supported by the National Natural Science Foundation of China (No. 11975012); the Outstanding Youth Project of Taizhou University (Grant No. 2019JQ002); and the Zhejiang Provincial Natural Science Foundation of China (Grant No. Y23A040001).

Institutional Review Board Statement: Not applicable.

Informed Consent Statement: Not applicable.

Data Availability Statement: Not applicable.

Conflicts of Interest: The authors declare no conflict of interest.

References

1. Yuan, H.; Yang, Y.; Guo, F.; Wang, J.; Cui, Z. Influence of multiphoton resonance excitation on the above-threshold ionization of a hydrogen atom. *Opt. Express* **2022**, *30*, 19745–19756. [CrossRef] [PubMed]
2. Chen, J.; Luan, Z.; Zhou, Q.; Alzahrani, A.K.; Biswas, A.; Liu, W. Periodic soliton interactions for higher-order nonlinear Schrodinger equation in optical fibers. *Nonlinear Dyn.* **2020**, *100*, 2817–2821. [CrossRef]
3. Chen, J.; Liu, M.; Liu, X.; Ouyang, Y.; Liu, W.; Wei, Z. The SnSSe SA with high modulation depth for passively Q-switched fiber laser. *Nanophotonics* **2020**, *9*, 2549–2555. [CrossRef]
4. Sun, T.; Zhang, S.W.; Wang, R.; Feng, S.; Liu, Y.; Lv, H.; Xu, H.F. Ionic Angular Distributions Induced by Strong-Field Ionization of Tri-Atomic Molecules. *Chin. Phys. Lett.* **2020**, *37*, 043301. [CrossRef]
5. Sun, T.; Yang, T.; Xu, H.; Wu, X.; Yu, T.; Zhou, X. Enhanced single-photon double ionization near threshold of substituted benzenes by synchrotron radiation. *Chem. Phys. Lett.* **2021**, *785*, 139144. [CrossRef]
6. Jiang, S.; Chen, J.; Wei, H.; Yu, C.; Lu, R.; Lin, C.D. Role of the Transition Dipole Amplitude and Phase on the Generation of Odd and Even High-Order Harmonics in Crystals. *Phys. Rev. Lett.* **2018**, *120*, 253201. [CrossRef] [PubMed]
7. Zhao, Y.T.; Jiang, S.C.; Zhao, X.; Chen, J.G.; Yang, Y.J. Effect of interband polarization on a solid's high-order-harmonic generation just belowthe band gap. *Opt. Lett.* **2020**, *45*, 2874–2877. [CrossRef] [PubMed]
8. Zhao, X.; Wang, S.J.; Yu, W.W.; Wei, H.; Wei, C.; Wang, B.; Chen, J.; Lin, C.D. Metrology of Time-Domain Soft X-Ray Attosecond Pulses and Reevaluation of Pulse Durations of Three Recent Experiments. *Phys. Rev. Appl.* **2020**, *13*, 034043. [CrossRef]

9. Nourbakhsh, Z.; Tancogne-Dejean, N.; Merdji, H.; Rubio, A. High Harmonics and Isolated Attosecond Pulses from MgO. *Phys. Rev. Appl.* **2021**, *15*, 014013. [CrossRef]
10. Zhou, S.S.; Lan, W.D.; Chen, J.G.; Wang, J.; Guo, F.M.; Yang, Y.J. High-order harmonic generation of 1-nonene under linearly polarized laser pulses. *Phys. Rev. A* **2022**, *106*, 023510. [CrossRef]
11. Corkum, P.B. Plasma perspective on strong field multiphoton ionization. *Phys. Rev. Lett.* **1993**, *71*, 1994–1997. [CrossRef] [PubMed]
12. Chen, J.; Yang, Y.; Chen, J.; Wang, B. Probing dynamic information and spatial structure of Rydberg wave packets by harmonic spectra in a few-cycle laser pulse. *Phys. Rev. A* **2015**, *91*, 043403. [CrossRef]
13. Ghimire, S.; DiChiara, A.D.; Sistrunk, E.; Agostini, P.; DiMauro, L.F.; Reis, D.A. Observation of high-order harmonic generation in a bulk crystal. *Nat. Phys.* **2011**, *7*, 138–141. [CrossRef]
14. Yan, J.Z.; Zhao, S.S.; Lan, W.D.; Li, S.Y.; Zhou, S.S.; Chen, J.G.; Zhang, J.Y.; Yang, Y.J. Calculation of high-order harmonic generation of atoms and molecules by combining time series prediction and neural networks. *Opt. Express* **2022**, *30*, 35444–35456. [CrossRef]
15. Qiao, Y.; Wu, D.; Chen, J.G.; Wang, J.; Guo, F.M.; Yang, Y.J. High-order harmonic generation from H_2^+ irradiated by a co-rotating two-color circularly polarized laser field. *Phys. Rev. A* **2019**, *100*, 063428. [CrossRef]
16. Li, P.; Gao, N.; Yu, R.X.; Wang, J.; Li, S.Y.; Guo, F.M.; Yang, Y.J. Amplitude and rotation of the ellipticity of harmonics from a linearly polarized laser field. *Chin. Phys. B* **2022**, *31*, 103303. [CrossRef]
17. Qiao, Y.; Wang, J.; Yan, Y.; Song, S.; Chen, Z.; Liu, A.; Chen, J.; Guo, F.; Yang, Y. Tunable spectral shift of high-order harmonic generation in atoms using a sinusoidally phase-modulated pulse. *Chin. Phys. B* **2022**, *31*, 064214. [CrossRef]
18. Yue, L.; Gaarde, M.B. Imperfect Recollisions in High-Harmonic Generation in Solids. *Phys. Rev. Lett.* **2020**, *124*, 153204. [CrossRef]
19. Lang, Y.; Peng, Z.; Liu, J.; Zhao, Z.; Ghimire, S. Proposal for High-Energy Cutoff Extension of Optical Harmonics of Solid Materials Using the Example of a One-Dimensional ZnO Crystal. *Phys. Rev. Lett.* **2022**, *129*, 167402. [CrossRef]
20. You, Y.S.; Wu, M.; Yin, Y.; Chew, A.; Ren, X.; Gholam-Mirzaei, S.; Browne, D.A.; Chini, M.; Chang, Z.; Schafer, K.J.; et al. Laser waveform control of extreme ultraviolet high harmonics from solids. *Opt. Lett.* **2017**, *42*, 1816–1819. [CrossRef]
21. Jiang, S.; Gholam-Mirzaei, S.; Crites, E.; Beetar, J.E.; Singh, M.; Lu, R.; Chini, M.; Lin, C.D. Crystal symmetry and polarization of high-order harmonics in ZnO. *J. Phys. B At. Mol. Opt. Phys.* **2019**, *52*, 225601. [CrossRef]
22. Tang, D.; Bian, X.B. Control of high-order harmonic generation in solids by orthogonally polarized laser fields. *Phys. Rev. B* **2021**, *104*, 104302. [CrossRef]
23. Kilen, I.; Kolesik, M.; Hader, J.; Moloney, J.V.; Huttner, U.; Hagen, M.K.; Koch, S.W. Propagation Induced Dephasing in Semiconductor High-Harmonic Generation. *Phys. Rev. Lett.* **2020**, *125*, 083901. [CrossRef]
24. Xia, P.; Kim, C.; Lu, F.; Kanai, T.; Akiyama, H.; Itatani, J.; Ishii, N. Nonlinear propagation effects in high harmonic generation in reflection and transmission from gallium arsenide. *Opt. Express* **2018**, *26*, 29393–29400. [CrossRef] [PubMed]
25. Li, F.; Li, N.; Liu, P.; Wang, Z. High-order harmonic generation from the interference of intra-cycle trajectories in the k-space. *Opt. Express* **2022**, *30*, 10280–10292. [CrossRef] [PubMed]
26. Langer, F.; Hohenleutner, M.; Huttner, U.; Koch, S.W.; Kira, M.; Huber, R. Symmetry-controlled temporal structure of high-harmonic carrier fields from a bulk crystal. *Nat. Photonics* **2017**, *11*, 227–231. [CrossRef]
27. Schubert, O.; Hohenleutner, M.; Langer, F.; Urbanek, B.; Lange, C.; Huttner, U.; Golde, D.; Meier, T.; Kira, M.; Koch, S.W.; et al. Sub-cycle control of terahertz high-harmonic generation by dynamical Bloch oscillations. *Nat. Photonics* **2014**, *8*, 119–123. [CrossRef]
28. Lü, L.J.; Bian, X.B. Ultrafast intraband electron dynamics of preexcited SiO_2. *Opt. Express* **2020**, *28*, 13432–13442. [CrossRef]
29. Yu, C.; Zhang, X.; Jiang, S.; Cao, X.; Yuan, G.; Wu, T.; Bai, L.; Lu, R. Dependence of high-order-harmonic generation on dipole moment in SiO_2 crystals. *Phys. Rev. A* **2016**, *94*, 013846. [CrossRef]
30. Lanin, A.A.; Stepanov, E.A.; Fedotov, A.B.; Zheltikov, A.M. Mapping the electron band structure by intraband high-harmonic generation in solids. *Optica* **2017**, *4*, 516–519. [CrossRef]
31. He, Y.L.; Guo, J.; Gao, F.Y.; Liu, X.S. Dynamical symmetry and valley-selective circularly polarized high-harmonic generation in monolayer molybdenum disulfide. *Phys. Rev. B* **2022**, *105*, 024305. [CrossRef]
32. Cao, J.; Li, F.; Bai, Y.; Liu, P.; Li, R. Inter-half-cycle spectral interference in high-order harmonic generation from monolayer MoS_2. *Opt. Express* **2021**, *29*, 4830–4841. [CrossRef] [PubMed]
33. Yu, C.; Jiang, S.; Wu, T.; Yuan, G.; Wang, Z.; Jin, C.; Lu, R. Two-dimensional imaging of energy bands from crystal orientation dependent higher-order harmonic spectra in $h-$BN. *Phys. Rev. B* **2018**, *98*, 085439. [CrossRef]
34. Jiang, S.; Wei, H.; Chen, J.; Yu, C.; Lu, R.; Lin, C.D. Effect of transition dipole phase on high-order-harmonic generation in solid materials. *Phys. Rev. A* **2017**, *96*, 053850. [CrossRef]
35. Feng, Y.; Shi, S.; Li, J.; Ren, Y.; Zhang, X.; Chen, J.; Du, H. Semiclassical analysis of ellipticity dependence of harmonic yield in graphene. *Phys. Rev. A* **2021**, *104*, 043525. [CrossRef]
36. Ndabashimiye, G.; Ghimire, S.; Wu, M.X.; Browne, D.A.; Schafer, K.J.; Gaarde, M.B.; Reis, D.A. Solid-state harmonics beyond the atomic limit. *Nature* **2016**, *534*, 520–523. [CrossRef]
37. Nefedova, V.E.; Fröhlich, S.; Navarrete, F.; Tancogne-Dejean, N.; Franz, D.; Hamdou, A.; Kaassamani, S.; Gauthier, D.; Nicolas, R.; Jargot, G.; et al. Enhanced extreme ultraviolet high-harmonic generation from chromium-doped magnesium oxide. *Appl. Phys. Lett.* **2021**, *118*, 201103. [CrossRef]

38. Huang, T.; Zhu, X.; Li, L.; Liu, X.; Lan, P.; Lu, P. High-order-harmonic generation of a doped semiconductor. *Phys. Rev. A* **2017**, *96*, 043425. [CrossRef]
39. Almalki, S.; Parks, A.M.; Bart, G.; Corkum, P.B.; Brabec, T.; McDonald, C.R. High harmonic generation tomography of impurities in solids: Conceptual analysis. *Phys. Rev. B* **2018**, *98*, 144307. [CrossRef]
40. Du, T.Y.; Tang, D.; Huang, X.H.; Bian, X.B. Multichannel high-order harmonic generation from solids. *Phys. Rev. A* **2018**, *97*, 043413. [CrossRef]
41. Ikemachi, T.; Shinohara, Y.; Sato, T.; Yumoto, J.; Kuwata-Gonokami, M.; Ishikawa, K.L. Trajectory analysis of high-order-harmonic generation from periodic crystals. *Phys. Rev. A* **2017**, *95*, 043416. [CrossRef]
42. Li, J.; Fu, S.; Wang, H.; Zhang, X.; Ding, B.; Hu, B.; Du, H. Limitations of the single-active-electron approximation in quantum simulations of solid high-order harmonic generation. *Phys. Rev. A* **2018**, *98*, 043409. [CrossRef]
43. Luu, T.T.; Wörner, H.J. Measurement of the Berry curvature of solids using high-harmonic spectroscopy. *Nat. Commun.* **2018**, *9*, 916. [CrossRef] [PubMed]
44. Liu, H.Z.; Li, Y.L.; You, Y.S.; Ghimire, S.; Heinz, T.F.; Reis, D.A. High-harmonic generation from an atomically thin semiconductor. *Nat. Phys.* **2017**, *13*, 262–265. [CrossRef]
45. Li, L.; Lan, P.; He, L.; Cao, W.; Zhang, Q.; Lu, P. Determination of Electron Band Structure using Temporal Interferometry. *Phys. Rev. Lett.* **2020**, *124*, 157403. [CrossRef] [PubMed]
46. Shao, T.J.; Lü, L.J.; Liu, J.Q.; Bian, X.B. Quantum path interferences and selection in interband solid high-order harmonic generation in MgO crystals. *Phys. Rev. A* **2020**, *101*, 053421. [CrossRef]
47. Vampa, G.; Hammond, T.J.; Thiré, N.; Schmidt, B.E.; Légaré, F.; McDonald, C.R.; Brabec, T.; Klug, D.D.; Corkum, P.B. All-Optical Reconstruction of Crystal Band Structure. *Phys. Rev. Lett.* **2015**, *115*, 193603. [CrossRef]
48. Bai, Y.; Fei, F.C.; Wang, S.; Li, N.; Li, X.L.; Song, F.Q.; Li, R.X.; Xu, Z.Z.; Liu, P. High-harmonic generation from topological surface states. *Nat. Phys.* **2021**, *17*, 311–315. [CrossRef]
49. Chacón, A.; Kim, D.; Zhu, W.; Kelly, S.P.; Dauphin, A.; Pisanty, E.; Maxwell, A.S.; Picón, A.; Ciappina, M.F.; Kim, D.E.; et al. Circular dichroism in higher-order harmonic generation: Heralding topological phases and transitions in Chern insulators. *Phys. Rev. B* **2020**, *102*, 134115. [CrossRef]
50. Vampa, G.; McDonald, C.R.; Orlando, G.; Corkum, P.B.; Brabec, T. Semiclassical analysis of high harmonic generation in bulk crystals. *Phys. Rev. B* **2015**, *91*, 064302. [CrossRef]
51. Zhao, Y.T.; Xu, X.Q.; Jiang, S.C.; Zhao, X.; Chen, J.G.; Yang, Y.J. Cooper minimum of high-order harmonic spectra from an MgO crystal in an ultrashort laser pulse. *Phys. Rev. A* **2020**, *101*, 033413. [CrossRef]
52. Jiang, S.; Yu, C.; Chen, J.; Huang, Y.; Lu, R.; Lin, C.D. Smooth periodic gauge satisfying crystal symmetry and periodicity to study high-harmonic generation in solids. *Phys. Rev. B* **2020**, *102*, 155201. [CrossRef]
53. Tancogne-Dejean, N.; Mücke, O.; Kärtner, F.; Rubio, A. Ellipticity dependence of high-harmonic generation in solids originating from coupled intraband and interband dynamics. *Nat. Commun.* **2017**, *8*, 745. [CrossRef] [PubMed]
54. Vampa, G.; McDonald, C.R.; Orlando, G.; Klug, D.D.; Corkum, P.B.; Brabec, T. Theoretical Analysis of High-Harmonic Generation in Solids. *Phys. Rev. Lett.* **2014**, *113*, 073901. [CrossRef]
55. Navarrete, F.; Ciappina, M.F.; Thumm, U. Crystal-momentum-resolved contributions to high-order harmonic generation in solids. *Phys. Rev. A* **2019**, *100*, 033405. [CrossRef]
56. Lauritzen, B.; Timoney, N.; Gisin, N.; Afzelius, M.; de Riedmatten, H.; Sun, Y.; Macfarlane, R.M.; Cone, R.L. Spectroscopic investigations of Eu^{3+}:Y_2SiO_5 for quantum memory applications. *Phys. Rev. B* **2012**, *85*, 115111. [CrossRef]
57. Theisen, M.; Linke, M.; Kerbs, M.; Fidder, H.; Madjet, M.E.A.; Zacarias, A.; Heyne, K. Femtosecond polarization resolved spectroscopy: A tool for determination of the three-dimensional orientation of electronic transition dipole moments and identification of configurational isomers. *J. Chem. Phys.* **2009**, *131*, 124511. [CrossRef]
58. Mu, T.; Chen, S.; Zhang, Y.; Guo, P.; Chen, H. Determining the orientation of transition moments and depolarization by fluorescence polarizing angle spectrum. *Opt. Express* **2015**, *23*, 11748–11754. [CrossRef]
59. Zhao, Y.T.; Ma, S.Y.; Jiang, S.C.; Yang, Y.J.; Zhao, X.; Chen, J.G. All-optical reconstruction of k-dependent transition dipole moment by solid harmonic spectra from ultrashort laser pulses. *Opt. Express* **2019**, *27*, 34392–34404. [CrossRef]
60. Qiao, Y.; Huo, Y.Q.; Jiang, S.C.; Yang, Y.J.; Chen, J.G. All-optical reconstruction of three-band transition dipole moments by the crystal harmonic spectrum from a two-color laser pulse. *Opt. Express* **2022**, *30*, 9971–9982. [CrossRef]
61. Wu, D.; Li, L.; Zhan, Y.; Huang, T.; Cui, H.; Li, J.; Lan, P.; Lu, P. Determination of transition dipole moments of solids with high-order harmonics driven by multicycle ultrashort pulses. *Phys. Rev. A* **2022**, *105*, 063101. 063101. [CrossRef]
62. Uchida, K.; Pareek, V.; Nagai, K.; Dani, K.M.; Tanaka, K. Visualization of two-dimensional transition dipole moment texture in momentum space using high-harmonic generation spectroscopy. *Phys. Rev. B* **2021**, *103*, L161406. [CrossRef]
63. Hoang, V.H.; Le, A.T. Factorization of high-order-harmonic-generation yields in impurity-doped materials. *Phys. Rev. A* **2020**, *102*, 023112. [CrossRef]